Design of Wideband Planar Linear-Circular Polarization Converter with Centrosymmetric Dual-Loop Elements

Peng Fei[1, *], Wei Hu[2], Weihua Guo[1], and Xin Wen[1]

Abstract—A wideband planar linear-circular polarization converter comprising periodic centrosymmetric dual-loop unit cells with wideband property is presented in this paper. Full-wave simulation and a parameter study are conducted to demonstrate the basic working principle of the converter. The performance of the device under oblique and deflected incidence situations is considered and discussed, and a prototype is manufactured and tested. Measured results show that the working band of the device covers 19.3 GHz to 31.8 GHz with less than 3 dB axial ratio, which agrees well with the simulated ones and thus validates the design concept.

1. INTRODUCTION

Circular polarization (CP) wave is widely used in satellite communication, radar, and remote sensing applications because it suffers less from multipath interference, rain echo, ionospheric attenuation, atmospheric absorption, and reflection effects than linearly polarized (LP) wave. However, generating a CP wave in a wide frequency band is challenging. One conventionally employed method is inserting an LP-CP converter on top of an LP antenna or antenna array.

A polarization converter is a reflective or transmissive polarization control device that can convert one polarization into its orthogonal component or perform transition between LP and CP [1–8]. For the LP-CP converter, one interesting early design was printed meander-line polarizer (MLP) [9, 10]. MLPs usually employ a multilayer structure, and spacers with low permittivity are necessary to maintain the desired distances between layers. In recent years, various kinds of wideband transmissive multilayer [11–17] and 3D [18, 19] LP-CP converters based on split-ring resonators [11, 13], frequency selective surfaces (FSSs) [12, 15, 16], and metamaterials [14, 17, 18] have been proposed.

Low-profile planar CP converters with single-layer structures have been investigated to further reduce the thickness of converters. In [20–22], Euler et al. presented different kinds of LP-CP converters that are based on FSSs. The 3 dB axial ratio (AR) bandwidths reached 21.1%. In [23], the operating principle and closed-form design formulas of a single-layer slotted FSS converter were discussed. In [24–26], Akgol et al. designed several metasurface polarization converters whose 3 dB AR bandwidth varied from 5.8% to 20%. In [27–29], several integrated designs of single-layer LP-CP converters and LP antennas, apart from isolated converters, were proposed for producing CP waves. In [27], a CP converter using a single-layer metamaterial was presented. The measured 3 dB AR bandwidth was approximately 17%. The device was also applied in an LP microstrip patch antenna as a superstrate, facilitating the radiation of the CP wave of this antenna composite in a frequency range of 13.55 GHz to 13.9 GHz (2.5%). Zhu et al. proposed an integrated design of a microstrip LP antenna covered by a metasurface CP converter, and the realized 3 dB AR bandwidth reached 9.3% [28]. In [29], a wide relative bandwidth

of 20% was achieved by integrating a corner-cut square metasurface single-layer structure with an LP slot antenna.

According to these works, 3 dB AR bandwidths of single-layer designs are usually limited to approximately 20%, which is insufficient for many wideband applications. Some wideband single-layer LP-CP converters have been previously introduced [30, 31]. Additional details regarding the design in [31] are provided in the current paper. Numerical analysis and a parameter study are conducted to investigate the working principle of the converters. Moreover, non-45° normal incidence situations are considered and discussed. Results indicate that the proposed device competently transmits incident LP waves into CP ones in a wide spectrum ranging from 19.3 GHz to 31.8 GHz (48.9%) with less than 3 dB AR maintaining approximately 3 dB insertion loss (IL).

The paper is arranged in the following manner. Section 2 presents the design of the converter, including the principle of operation, parameter study, and oblique and deflected incidence analysis. Section 3 discusses the experimental results, and Section 4 provides the conclusion.

2. DESIGN OF THE LP-CP CONVERTER

2.1. Principle of Operation

Figures 1(a) and (b) demonstrate the proposed converter, which is periodic in configuration. The unit cell is composed of two centrosymmetric metallic loops connected by a strip line in the central axis. The unit cell width and height are W and L, respectively. The loop width and height are s and H, respectively. The width of the metallic strip is d. The structure is etched on the commonly used Rogers RT/Duroid 5880 laminate with a thickness t of 0.254 mm and substrate relative permittivity ε_r equal to 2.2.

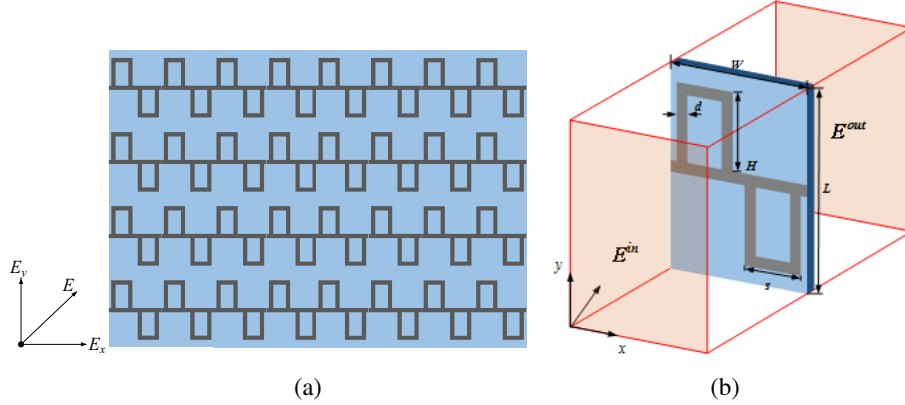(a)   (b)

Figure 1. Configuration of the proposed converter.

The Floquet mode simulation model of the unit cell is illustrated in Figure 1(b). A planar electric field can be resolved into a pair of components, namely, E_x and E_y, orthogonally with each other. Assuming that the incident LP wave E^{in} is oriented at 45° to the x-axis as shown in Figure 1(b), then $|E_x^{in}|/|E_y^{in}| = 1$ and $\angle(E_x^{in}) - \angle(E_y^{in}) = 0$. Define

$$\beta = |E_x| / |E_y|, \tag{1}$$
$$\delta = \angle(E_y) - \angle(E_x). \tag{2}$$

For E^{out}, the perfect CP wave is produced when

$$\beta = 1, \tag{3}$$
$$\delta = n \cdot 90° (n = \pm 1, 3, 5 \ldots). \tag{4}$$

However, achieving the perfect CP is difficult because it can be realized in a narrow frequency band only. AR is used to measure the degree of polarization, which can be defined by β and δ as

$$\text{AR} = \left[\frac{1 + \beta^2 + \sqrt{(1 - \beta^2)^2 + 4\beta^2 \cos^2 \delta}}{1 + \beta^2 - \sqrt{(1 - \beta^2)^2 + 4\beta^2 \cos^2 \delta}} \right]^{\frac{1}{2}}. \tag{5}$$

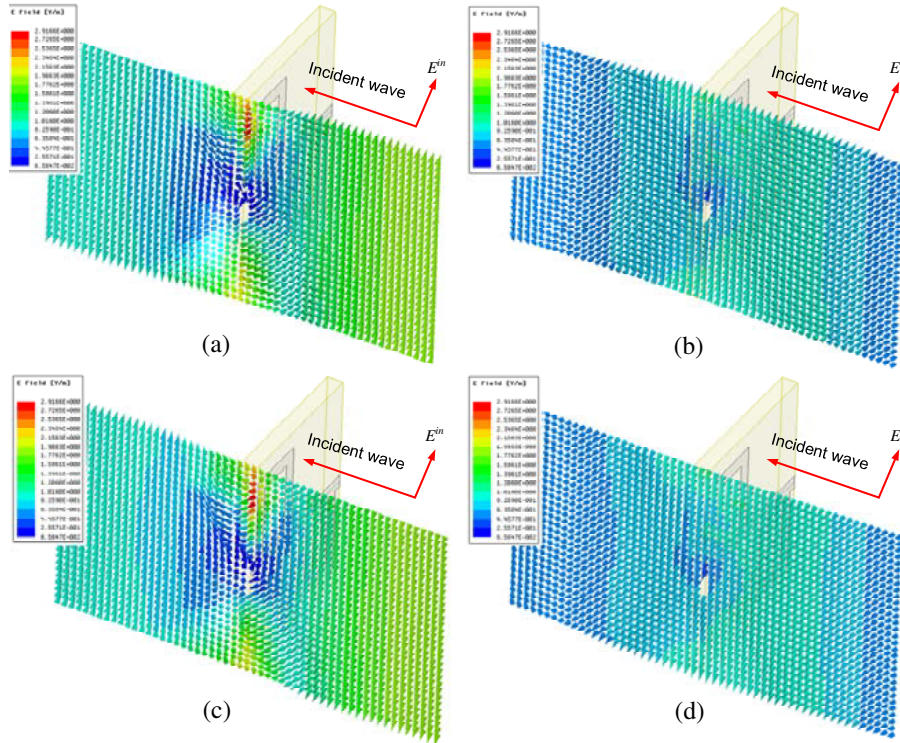For perfect CP, AR is equal to 1 (or 0 dB). In most cases, CP waves with less than 3 dB AR are considered acceptable.

Figure 2. Electric field distributions at (a) $\omega t = 0°$, (b) $\omega t = 90°$, (c) $\omega t = 180°$, and (d) $\omega t = 270°$.

Figure 2 shows the electric field distributions with 45° normal incident LP wave for $\omega t = 0°$, 90°, 180°, and 270°. The electric field distribution of the incident side is the superposition of the incident and reflected waves. By contrast, the electric field of the transmitted side shows 90° rotation as ωt increases by 90°, which confirms the CP operation of the proposed polarizer. The surface current distribution of the unit cell is also simulated to elucidate the physical mechanism of the polarization conversion. Figure 3(a) shows the surface current distribution with E_x illumination. As shown in the figure, the surface currents are dense on the central axis strip but sparse and out of phase on the vertical arms of the loops. In this case, the structure is inductive to E_x and delays its phase. Figure 3(b) presents the surface current distribution under E_y illumination. In this case, the currents are dense and in phase on the vertical arms of the loops, which indicates that the structure is capacitive to E_y and thus advances the phase of E_y. From Figure 2, the polarization converter can be regarded as a lumped network that simultaneously operates as a phase delayer to E_x^{out} and a phase advancer to E_y^{out}. If the two components of E^{out} have equal amplitude and quadrature phase, then the incident LP wave will be converted into a CP wave.

Figure 4 shows the normalized power of transmitted co-polarization, transmitted cross-polarization, reflected co-polarization, and reflected cross-polarization with 45° normal incident LP wave. From the figure, approximately −3 dB power passes through the converter with desired co-polarization while another approximately −3 dB power is reflected in the form of cross-polarization. From the view of
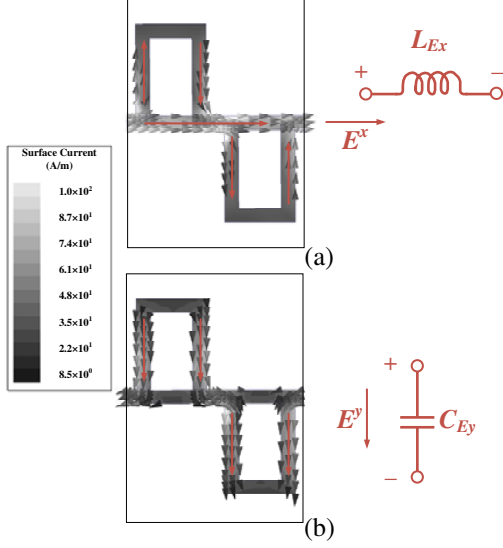
Figure 3. Current distribution: (a) E_x illumination and (b) E_y illumination.
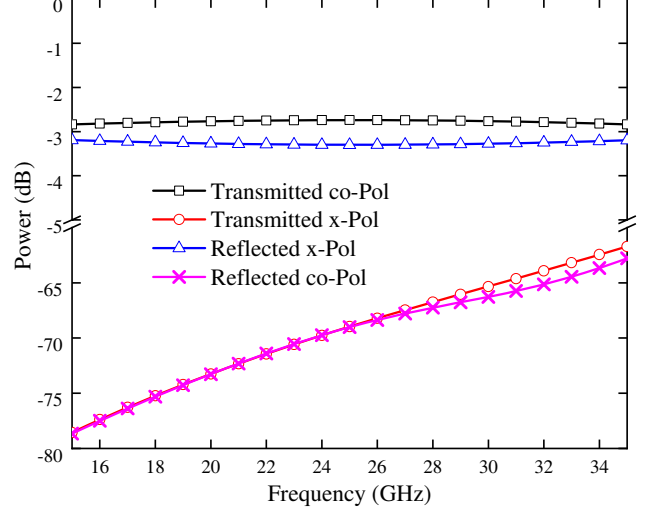

Figure 4. Normalized power of transmitted co-polarization, transmitted cross-polarization, reflected co-polarization, and reflected cross-polarization.

impedance matching between free space and the proposed structure, the converter can be regarded as a polarization-selective device, which allows the desired CP wave to pass through while rejecting the undesired one.

2.2. Parametric Study

The geometrical parameters are studied in this section. β and δ, and IL and AR are used to evaluate the effects of each parameter on the converter. Herein, IL is defined in dB as

$$\text{IL} = 10 \cdot \log_{10} \frac{\left|E^{out}\right|^2}{\left|E^{in}\right|^2} = -\left|S_{21}\right|. \tag{6}$$

Figure 5 shows the performance of the converter when L, which denotes the height of the cell, varies from 3 mm to 4 mm. As shown in the figure, the value of δ increases from 70° to 96° as the value of L varies from 3 mm to 4 mm; the curve of β becomes flat as the value of L increases. The two preceding factors result in a small extremum of the AR curve and a large slope in and around 25 GHz when the value of L decreases but lead to a large extremum and a small slope when the value of L increases. By contrast, the increase in the value of L also results in reduced IL, which can be simply explained by the decrease in metal area ratio. Figure 6 depicts the variation of β, δ, IL, and AR with different heights of loop H. First, the value of δ rises as heights of the loop increase due to the increment of C_{Ey} shown in Figure 3(b). Moreover, the value of β decreases and IL increases as the value of H increases, suggesting that additional E_x energy is blocked when the loop expands in the y dimension. The figure also shows that the minimum AR shifts to high frequencies when the value of H decreases, which can be explained by the size reduction of the loop. Figure 7 shows the performance of the converter with different metal strip widths d. The increase of strip width increases L_{Ex}, thus resulting in a large δ. In addition, the increase in metal strip width causes large β and IL, indicating that more E_y energy is reflected compared with that in E_y. In terms of AR, the minimum AR and the widest < 3 dB AR bandwidth are achieved when $d = 0.2$ mm, in which case the values of β and δ come to a compromise in the entire working band.

Figures 8 and 9 show β and δ, and IL and AR variations with different values of s and W, respectively. As suggested in the figures, the performance of the converter is less sensitive to the
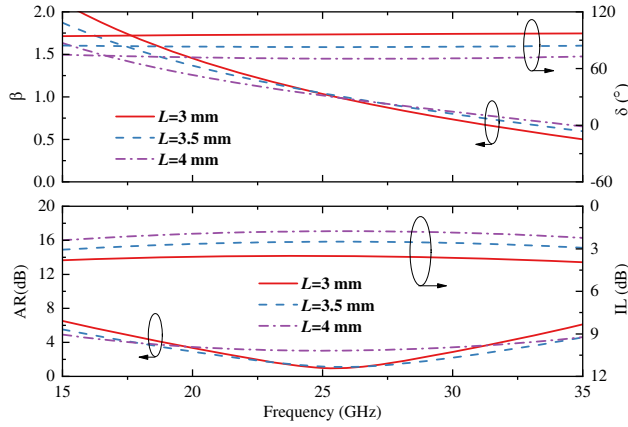
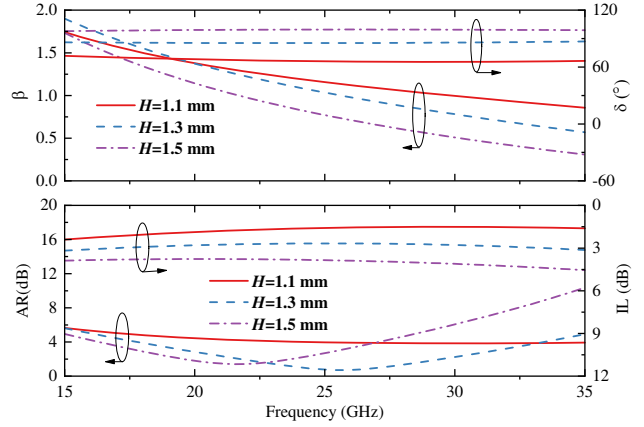**Figure 5.** Variation of β, δ, IL, and AR with different values of L.

Figure 6. Variation of β, δ, IL, and AR with different values of H.
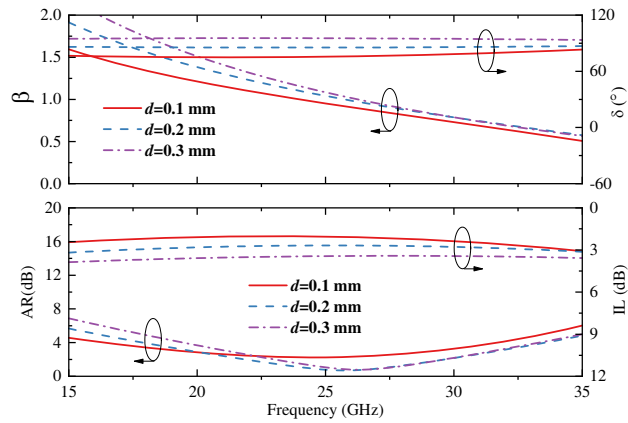
Figure 7. Variation of β, δ, IL, and AR with different values of d.
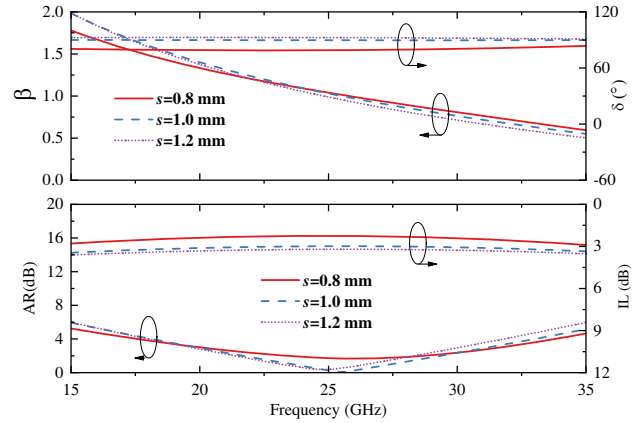

Figure 8. Variation of β, δ, IL, and AR with different values of s.

Table 1. Dimensions of the proposed LP-CP converter.

Parameters	Length (in mm)
L	3.35
W	2.5
s	1
H	1.4
d	0.2

variations of s and W compared with that of other parameters, such as L, H, and d. A set of optimized dimensions is obtained by full-wave simulation, as listed in Table 1.

2.3. Oblique and Deflected Incidence Analysis

In the previous section, discussions are based on the 45° polarized incident wave. However, in practice, the incident wave on the converter may be oblique or deflected due to the antenna radiation distortion or inaccurate installation. Three typical non-45° incidences are shown in Figure 10 with mismatch angles
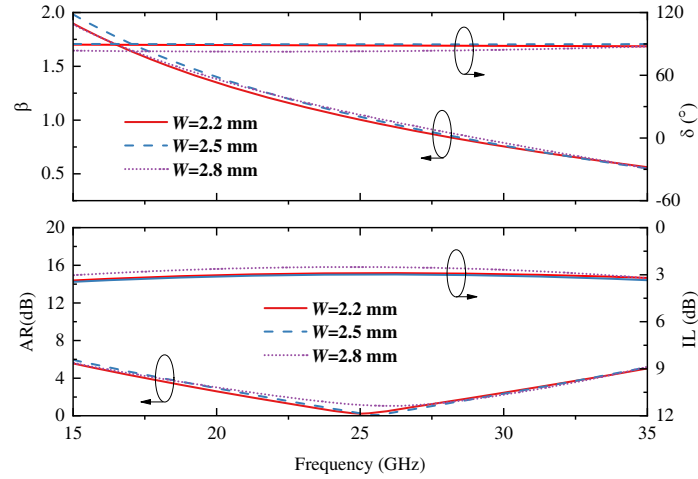
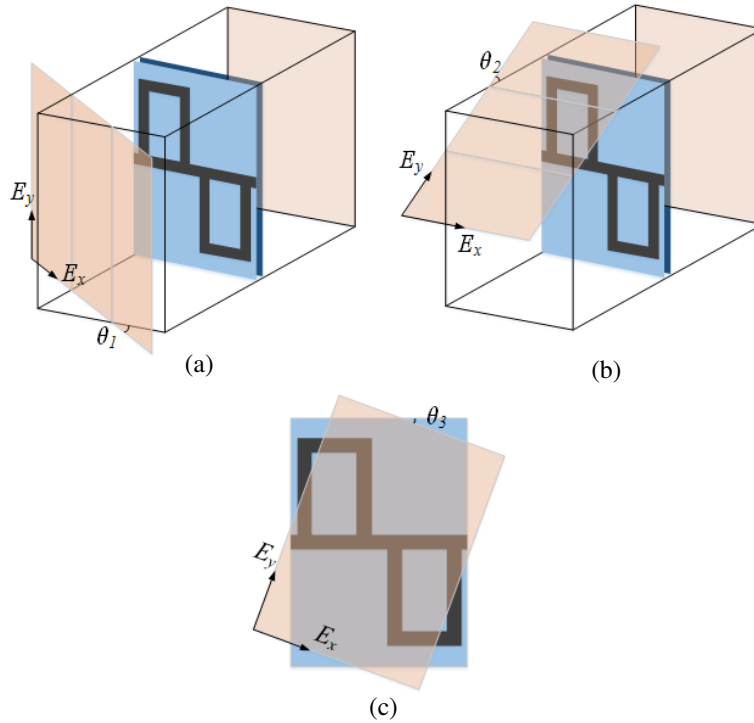**Figure 9.** Variation of β, δ, IL, and AR with different values of W.

Figure 10. Illustration of the non-45° incidence cases.

θ_1, θ_2, and θ_3. Figures 11(a) and (b) show the AR and IL variation with 0°–60° oblique incidence from different directions (as presented in the cases in Figures 10(a) and (b)). The solid red lines indicate the AR $\leq$ 3 dB or IL $\leq$ 3 dB range. From the figure, the two cases show symmetry in tendency; as the mismatch angle increases, the usable band shifts toward high and low frequencies. The figures also suggest that the converter is robust to oblique incidence, which has more than 11 GHz usable band with 30° oblique incidence. Figure 11(c) shows the variation of AR and IL with 0°–30° deflected incidence (as indicated in the cases in Figure 10(c)). The usable band is generally limited by the IL $\leq$ 3 dB bandwidth, which disappears when the mismatch angle increases to approximately 12°. However, the converter still has more than 10 GHz usable band with 7.5° deflected incidence.
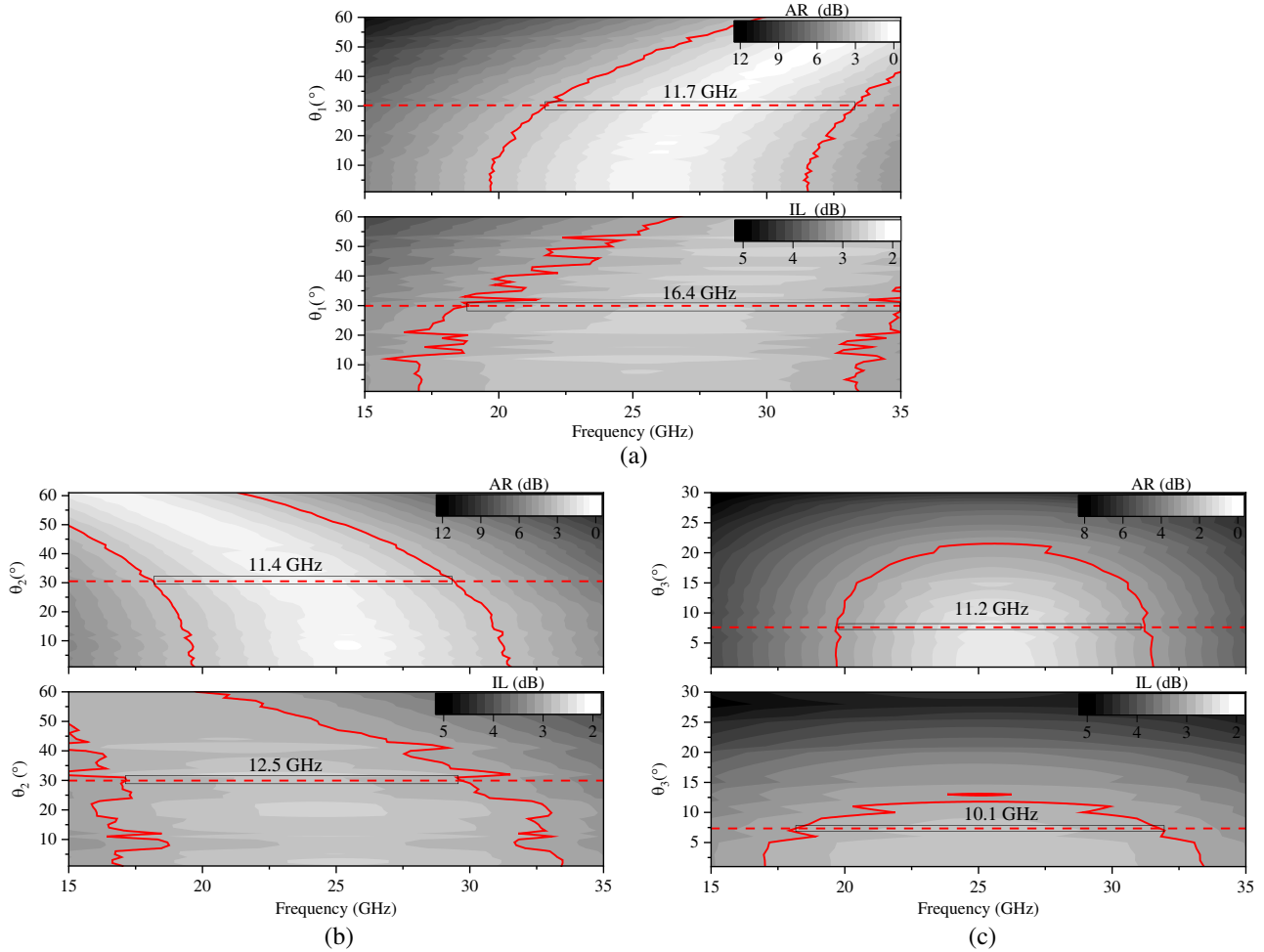
Figure 11. Variation of AR and IL with mismatch angles of (a) θ_1, (b) θ_2, and (c) θ_3.

3. RESULTS AND VERIFICATION

A round-shaped prototype with approximately 2400 elements is fabricated to verify the design concept. The prototype is measured in an anechoic chamber a by two-port VNA (Agilent E8363C) with transmitting and receiving horn antennas connected to both ports. The distance between antennas and the prototype d_f should satisfy the far-field condition, which is given by the following, to obtain an accurate measurement result:

$$d_f \geq \frac{2D^2}{\lambda} \tag{7}$$

where D is the largest dimension of the antenna, and λ is the minimum wavelength. In this case, $D = 41$ mm and $\lambda = 8.57$ mm; thus, d_f should be larger than 392.3 mm.

A sketch of the experimental setup is shown in Figure 12. The distance from each horn to the prototype is set to 600 mm, which is sufficient for the far-field condition. During the test process, the receiver horn rotates axially to measure the S_{21} data at various angles. Free space S_{21} data are also collected to calibrate the IL of the prototype. Notably, all the raw data are gated in the time domain to filter out the effect of mutual coupling and multipath reception. A photograph of the fabricated prototype and the measured IL and AR are shown in Figure 13. The measured results show reasonable agreement with the simulated ones. The discrepancies between the simulated and measured results may be attributed to fabrication inaccuracy and test environment scattering errors. The < 3 dB AR frequency band ranges from 19.3 GHz to 31.8 GHz with a relative bandwidth of 48.9%. The insertion

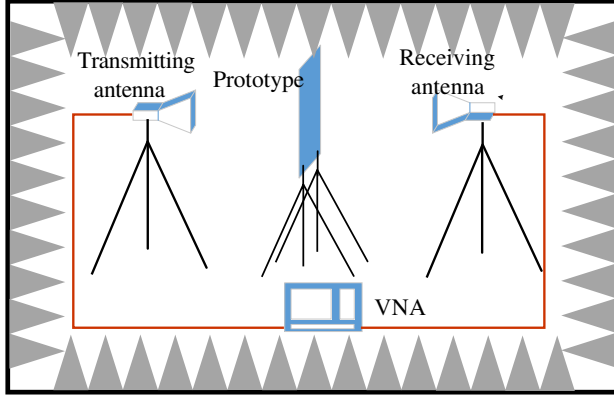loss is approximately 3 dB in the working frequency band.
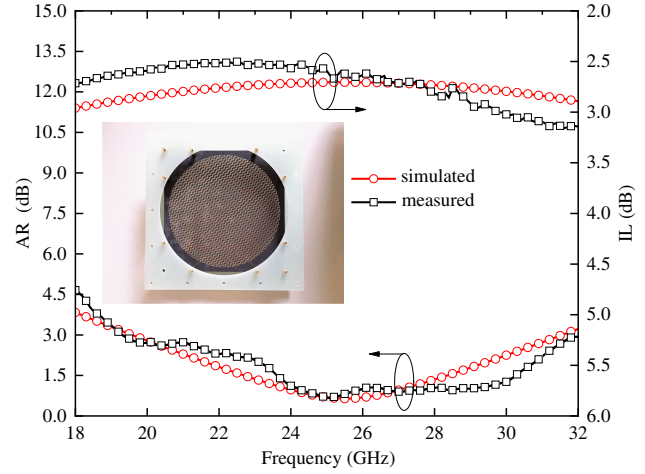

Figure 12. Sketch of the measurement setup.

Figure 13. Measured AR and IL.

4. CONCLUSION

A wideband single-layer LP-CP converter with a novel centrosymmetric dual-loop unit cell is proposed in this work, and a prototype is manufactured and tested. The measured $< 3\,\mathrm{dB}$ AR bandwidth reaches 48.9% with approximately 3 dB IL. In addition, the converter is robust to at least 30° oblique and 7.5° deflected incidence with more than 10 GHz bandwidth. The wide bandwidth, low profile, and robust performance of the proposed design highlight its integration potential with microwave and millimeter-wave conformal radome and antenna systems.

REFERENCES

1. Zhao, J. and Y. Cheng, "A high-efficiency and broadband reflective 90° linear polarization rotator based on anisotropic metamaterial," *Applied Physics B*, Vol. 122, No. 10, 255, 2016.
2. Zhao, J., Y. Cheng, and Z. Cheng, "Design of a photo-excited switchable broadband reflective linear polarization conversion metasurface for terahertz waves," *IEEE Photonics Journal*, Vol. 10, No. 1, 1–10, 2018.
3. Fang, C., Y. Cheng, Z. He, J. Zhao, and R. Gong, "Design of a wideband reflective linear polarization converter based on the ladder-shaped structure metasurface," *Optik*, Vol. 137, 148–155, 2017.
4. Cheng, Y. Z., C. Fang, X. S. Mao, R. Z. Gong, and L. Wu, "Design of an ultrabroadband and high-efficiency reflective linear polarization convertor at optical frequency," *IEEE Photonics Journal*, Vol. 8, No. 6, 1–9, 2016.
5. Zhao, J. C. and Y. Z. Cheng, "Ultra-broadband and high-efficiency reflective linear polarization convertor based on planar anisotropic metamaterial in microwave region," *Optik*, Vol. 136, 52–57, 2017.
6. Cheng, Y., R. Gong, and L. Wu, "Ultra-broadband linear polarization conversion via diode-like asymmetric transmission with composite metamaterial for terahertz waves," *Plasmonics*, Vol. 12, No. 4, 1113–1120, 2017.
7. Fartookzadeh, M., "Design of metamirrors for linear to circular polarization conversion with super-octave bandwidth," *Journal of Modern Optics*, Vol. 64, No. 18, 1854–1861, 2017.
8. Fartookzadeh, M., "Multi-band metamirrors for linear to circular polarization conversion with wideband and wide-angle performances," *Applied Physics B*, Vol. 123, No. 4, 115, 2017.

9. Chu, R. and K. Lee, "Analytical model of a multilayered meander-line polarizer plate with normal and oblique plane-wave incidence," *IEEE Transactions on Antennas and Propagation*, Vol. 35, 652–661, 1987.

10. Young, L., L. A. Robinson, and C. Hacking, "Meander-line polarizer," *IEEE Transactions on Antennas and Propagation*, Vol. 21, No. 3, 376–378, 1973.

11. Zhao, R., H.-Y. Chen, L. Zhang, F. Li, P. Zhou, J. Xie, and L.-J. Deng, "Design and implementation of high efficiency and broadband transmission-type polarization converter based on diagonal split-ring resonator," *Progress In Electromagnetics Research*, Vol. 161, 1–10, 2018.

12. Lin, B., J. Wu, X. Da, W. Li, and J. Ma, "A linear-to-circular polarization converter based on a second-order band-pass frequency selective surface," *Applied Physics A*, Vol. 123, No. 1, 43, 2017.

13. Cheng, Y., C. Wu, Z. Z. Cheng, and R. Z. Gong, "Ultra-compact multi-band chiral metamaterial circular polarizer based on triple twisted split-ring resonator," *Progress In Electromagnetics Research*, Vol. 155, 105–113, 2016.

14. Lin, B., J. Guo, B. Huang, L. Fang, P. Chu, and X. Liu, "Wideband linear-to-circular polarization conversion realized by a transmissive anisotropic metasurface," *Chinese Physics B*, Vol. 27, No. 5, 054204, 2018.

15. Zhang, W., J. Li, and J. Xie, "A broadband circular polarizer based on cross-shaped composite frequency selective surfaces," *IEEE Transactions on Antennas and Propagation*, Vol. 65, No. 10, 5623–5627, 2017.

16. Ericsson, A. and D. Sjöberg, "Design and analysis of a multilayer meander line circular polarization selective structure," *IEEE Transactions on Antennas and Propagation*, Vol. 65, No. 8, 4089–4101, 2017.

17. Li, Y., J. Zhang, S. Qu, J. Wang, L. Zheng, Y. Pang, Z. Xu, and A. Zhang, "Achieving wide-band linear-to-circular polarization conversion using ultra-thin bi-layered metasurfaces," *Journal of Applied Physics*, Vol. 117, No. 4, 044501, 2015.

18. Tamayama, Y., K. Yasui, T. Nakanishi, and M. Kitano, "A linear-to-circular polarization converter with half transmission and half reflection using a single-layered metamaterial," *Applied Physics Letters*, Vol. 105, No. 2, 021110, 2014.

19. Akbari, M., M. Farahani, A. Sebak, and T. A. Denidni, "Ka-band linear to circular polarization converter based on multilayer slab with broadband performance," *IEEE Access*, Vol. 5, 17927–17937, 2017.

20. Euler, M., V. Fusco, R. Cahill, and R. Dickie, "Comparison of frequency-selective screen-based linear to circular split-ring polarisation convertors," *IET Microwaves, Antennas & Propagation*, Vol. 4, No. 11, 1764–1772, 2010.

21. Euler, M., V. Fusco, R. Cahill, and R. Dickie, "325 GHz single layer sub-millimeter wave FSS based split slot ring linear to circular polarization convertor," *IEEE Transactions on Antennas and Propagation*, Vol. 58, No. 7, 2457–2459, 2010.

22. Euler, M., V. Fusco, R. Dickie, R. Cahill, and J. Verheggen, "Sub-mm wet etched linear to circular polarization FSS based polarization converters," *IEEE Transactions on Antennas and Propagation*, Vol. 59, No. 8, 3103–3106, 2011.

23. Wang, J., W. Wu, and Z. Shen, "Improved polarization converter using symmetrical semi-ring slots," *2014 IEEE Antennas and Propagation Society International Symposium (APSURSI)*, 2052–2053, 2014.

24. Altintas, O., E. Unal, O. Akgol, M. Karaaslan, F. Karadag, and C. Sabah, "Design of a wide band metasurface as a linear to circular polarization converter," *Modern Physics Letters B*, Vol. 31, No. 30, 1750274, 2017.

25. Akgol, O., E. Unal, O. Altintas, M. Karaaslan, F. Karadag, and C. Sabah, "Design of metasurface polarization converter from linearly polarized signal to circularly polarized signal," *Optik*, Vol. 161, 12–19, 2018.

26. Akgol, O., O. Altintas, E. Unal, M. Karaaslan, and F. Karadag, "Linear to left-and right-hand circular polarization conversion by using a metasurface structure," *International Journal of Microwave and Wireless Technologies*, Vol. 10, No. 1, 133–138, 2018.

27. Ma, X., C. Huang, M. Pu, C. Hu, Q. Feng, and X. Luo, "Single-layer circular polarizer using metamaterial and its application in antenna," *Microwave and Optical Technology Letters*, Vol. 54, No. 7, 1770–1774, 2012.

28. Zhu, H., K. L. Chung, X. Sun, S. W. Cheung, and T. I. Yuk, "CP metasurfaced antennas excited by LP sources," *IEEE Antennas and Propagation Society International Symposium*, 1–2, 2012.

29. Huang, Y., L. Yang, J. Li, Y. Wang, and G. Wen, "Polarization conversion of metasurface for the application of wide band low-profile circular polarization slot antenna," *Applied Physics Letters*, Vol. 109, No. 5, 054101, 2016.

30. Fei, P., Z. Shen, X. Wen, and F. Nian, "A single-layer circular polarizer based on hybrid meander line and loop configuration," *IEEE Transactions on Antennas and Propagation*, Vol. 63, No. 10, 4609–4614, 2015.

31. Fei, P., X. Wen, P. Zhang, and W. Guo, "A wideband single-layered circular polarizer with centrosymmetric dual-loop elements," *2016 46th European Microwave Conference (EuMC)*, 1271–1274, 2016.